36G.0   CONTROL OF MICROSTRUCTURE DURING ADDITIVIE MANUFACTRUING OF NI ALLOYS

Ruben Ochoa (Mines)
Faculty: Amy Clarke (Mines) and Johan Klemm-Toole (Mines)
Industrial Mentor: Jeremy Iten (Elementum 3D), TBD

This project initiated in Fall 2021 and is supported by the Office of Naval Research. The research performed during this project will serve as the basis for a Ph.D. thesis program for Ruben Ochoa.

36G.1   Project Overview and Industrial Relevance

Nickel-based superalloys have a superior combination of mechanical properties with high toughness, corrosion resistance, and high-temperature strength, making them a key material for the aerospace, energy, and chemical industries [1]. These alloys also exhibit good weldability, depending on their content of γ', Ni3(Al, Ti, Ta, Nb). Due to their excellent mechanical properties and their weldability, nickel-based superalloys are a viable candidate for additive manufacturing (AM). It should be noted, however, that a system with high γ' will be more susceptible to hot cracking, due to larger solidification temperature range caused by the $\gamma - \gamma'$ eutectic. Since the eutectic has the lowest melting point, it will solidify last creating a liquid film around grain boundaries. As the system cools, these grains will shrink, creating a stress on the film causing it to rupture; with no more eutectic to back fill into the boundaries, this will serve as a crack initiation site [2]. Thus, the hot cracking issue must be addressed for AM to produce components with properties that are comparable to traditional manufacturing.

The marginally stable Ivantsov model coupled with a columnar to equiaxed transition (CET) model reveals a high solidification velocity and low thermal gradient will produce equiaxed grains, whereas a low velocity and high thermal gradient will result in columnar grains [3]. Under additive manufacturing conditions, a melt pool will produce columnar grains until it reaches sufficiently high solidification velocities and a sufficiently low gradient, at which point the CET will occur; this transition is usually seen at the top of the melt pool. These columnar grains are highly susceptibility to hot cracking, due to large regions of continuous grain boundary and anisotropic properties caused by the solidification texture. Thus, to eliminate hot cracking and promote isotropic mechanical behavior, the CET must be encouraged at higher temperature gradients and lower solidification velocities. This can be achieved by introducing inoculants into the melt that will serve as nucleation sites for equiaxed grains [4].

36G.2   Previous Work

36G.2.1 In-Situ AM Simulator Experiments

Laser powder bed fusion (L-PBF) conditions were simulated at the Advanced Photon Source (APS) at Argonne National Laboratory to capture transverse images of in-situ solidification of laser produced melt pools. Various nickel-based superalloys were tested, inducing IN738, IN718, CM 247 LC, and C276. Base materials were also varied between as-built, columnar, and inoculated conditions. Experiments included variations with a powder layer on top of the base material, bare base material, and inoculated powder on base material. Numerous laser powers were utilized, ranging from 54 to 486 Watts; both spot and raster scan strategies were simulated with raster speeds ranging from 0.5 to 2 m/s. These simulations produced x-ray radiography data, allowing for capture of in-situ solidification velocities at distinct solidification conditions, while producing different grain morphologies

36G.2.2 Haynes 230 Inoculation

The effectiveness of one inoculant type, called Inoculant A, on reducing hot cracking during Laser Powder Bed Fusion (L-PBF) of H230 was examined through the production of three L-PBF parts: one with no inoculation, one with 1wt% of Inoculant A, and one with 2.66wt% of Inoculant A. The cross section of each condition is shown in **Figure 36G.1**. The base case seen in **Figure 36G.1A** illustrates long cracks that are parallel to the build direction, signifying these solidification cracks are caused by the eutectic film being ruptured between columnar grains. The addition of 1wt% of Inoculant A eliminated the hot cracking, as seen in **Figure 36G.1B**. Increasing the inoculant content to 2.66wt% introduced more severe hot cracking than the base condition, as illustrated in **Figure 36G.1C**.

These cracks are much larger than the ones seen in the base case and are seen between build layers, not just between columnar gains. It is believed that a percentage of the inoculant may have been dissolved, changing the solute concentration and thus altering the crack susceptibility. The change in crack susceptibly as a function of amount of melted inoculant was determined by applying Kou's crack susceptibly index (CSI), as shown in **Equation 36G.1** [5]. This index compares the different thermal gradients near full solidification. A high index signifies a large temperature range for the final stages of solidification, making the system more susceptible to hot cracking. Five cases were tested for both 1wt% and 2.66wt%; starting at the base H230 composition and accommodating an increase of melted inoculants by 25% until all inoculants were melted. **Figure 36G.2** portrays that any amount of dissolved inoculant will cause an increase in crack susceptibly, however the most detrimental cases range from 0.5-0.75 grams melted. The 2.66wt% case likely had 25% of its inoculants melted, since it is likely that the 1wt% case also had melted inoculant, but this was not enough to severely affect crack susceptibly index.

$$CSI = |dT/d(f_s^{1/2})| \qquad \text{(36G.1)}$$

36G.3   Recent Progress

36G.3.1 Liquid/Solid interface tracking

An imageJ plug-in was utilized to manually track the solid/liquid interface of x-ray radiography obtained through the APS experiments. For spot melts, the interface is tracked starting when the laser shuts off until the melt pool is fully solidified. Raster melt tracking began once the melt pool reached its maximum size before the laser begins to travel. Nickel's high density is responsible creating low contrast between the solid and liquid phases in the x-ray radiography, making it difficult to track the solid/liquid interface on most frames. The interface was tracked every ten frames, creating a relative pixel position plot at different frames, as seen in **Figure 36G.3**. These plots are then converted to represent velocity vs frame by taking intercepts along y-axis, representing the mid-point. Examples of these plots are shown in **Figure 36G.4**, comparing velocity as a function of laser power (108, 216, and 324 Watts). **Figure 36G.4A** has few data points, because 108 Watts produced a small enough melt pool that it solidified within 40 frames. **Figure 36G.4B-C** both share trends illustrating the maximum velocity soon after solidifying begins, then becomes relatively constant until another increase is seen as solidification is near completion. The velocities are shown to increase as a function of laser power, making the nucleation of equiaxed grains more likely at higher powers. It is important to note that the software used to create these plots does not include the velocity of the first interface equaling zero. The spike in velocity seen as solidification begins is believed to an artifact of how the interfaces were tracked. The interface in the first few sets of frames were skipped due to low visibility. Thus, producing a larger distance between intercepts and creating a non-representative spike in velocity.

36G.3.2 Thermal Gradient Simulation

The computational fluid dynamics software, Flow3D, was utilized to model the melt pool dynamics of an APS spot weld. Flow3D has the capability of simulating fluid dynamics, multiple laser reflections, and rising gas caused by metal vaporization, allowing it to represent keyholing mode that may occur during melting. To streamline model validation, a spot weld was chosen over a raster due to its simpler geometry. Flow3D's data base included a data set for IN718, therefore spot melt on IN718 with a laser power of 216 Watts was modeled. The associated x-ray radiography illustrates the melt to be in keyholing mode. To match melt pool geometries, variables were adjusted including absorption rate, rising pressure, and evaporation accommodation; the final values are illustrated in **Table 36G.1**, along with other assumptions. Melt pool measurements were taken once the laser was shut off, at which point the melt had reached its maximum dimensions. The in-situ radiography and modeled dimensions are portrayed in **Figure 36G.5**. Although the dimensions vary by a few microns, the models mesh size of five microns place the dimensions within modeling error. However, more model tuning will be conducted to better match the melt pool shape. The simulation only utilized ten-time steps which limited the data points, thus the simulation is not fully representative of the APS experiment. To predict grain morphology, more work must be done to develop a solidification map of IN718 and to determine a more representative thermal gradient coupled with in-situ velocity measurements.

36G.3.3 Microstructural Analysis

To analyze grain morphologies as a function of solidification conditions, Election Backscatter Diffraction (EBSD) was performed on the transverse cross-section of various APS samples. To ensure the cross-section was taken as close to center as possible, top-down SEM images were taken to measure the center of each weld, as illustrated in **Figure 36G.6A**. These top-down images also provided information on surface dendrite orientation throughout the melt pool. **Figure 36G.6B** shows columnar dendrites traveling from the walls of the raster at an angle following the laser movement. The CET is observed near the center of raster, through equiaxed dendrites are present at the bottom of the image. EBSD analysis was conducted on three IN718 raster conditions at 216 Watts to observe the effects of inoculation. These conditions include mixes between columnar/inoculated bases and inoculated/non-inoculated powder. Mean inverse pole figure maps for the conditions are illustrated in **Figure 36G.7**. **Figure 36G.7A** exhibits the CET at a localized area near the top of the raster. Since the CET is not uniform throughout the top of the raster; it is believed the CET was induced by a powder particle that was disturbed during melting, landing on top of the melt and serving as a nucleation site. **Figure 36G.7B** reveals a uniform layer of equiaxed grains at the top of the raster, since the CET was induced by inoculation instead of loose powders. However, the sample still experienced strong solidification texture, as shown through the (100) concentration in its ODF plot, which is also seen in **Figure 36G.7A**. The microstructural effects of multiple inoculated layers are displayed in **Figure 36G.7C**. Due to its inoculation, each build layer will produce equiaxed grains throughout the top of the raster, serving as growth sites for the next build layers of columnar grains. This drastically refines the grain size and minimizes solidification texture.

36G.4   Plans for Next Reporting Period

- Perform additional Flow 3D simulations.
- Simulate melt pools with powder layers.
- Develop solidification processing maps and compare microstructural outcomes.
- Create CET models for different alloys and perform validation with EBSD results.

36G.5   References

[36G.1] T.M. Pollock, S. Tin, Nickel-based superalloys for advanced turbine engines: Chemistry, microstructure and properties, Journal of Propulsion and Power. 22 (2006) 361–374.

[36G.2] J. Xu, X. Lin, P. Guo, H. Dong, X. Wen, Q. Li, et al., The initiation and propagation mechanism of the overlapping zone cracking during laser solid forming of in-738lc superalloy, Journal of Alloys and Compounds. 749 (2018) 859–870.

[36G.3] W. Kurz, C. Bezençon, M. Gäumann, Columnar to equiaxed transition in solidification processing, Science and Technology of Advanced Materials. 2 (2001) 185–19.

[36G.4] Q. Han, Y. Gu, J. Huang, L. Wang, K.W.Q. Low, Q. Feng, et al., Selective laser melting of Hastelloy X nanocomposite: Effects of tic reinforcement on crack elimination and Strength Improvement, Composites Part B: Engineering. 202 (2020) 108442.

[36G.5] S. Kou, A criterion for cracking during solidification, Acta Materialia. 88 (2015) 366–374.
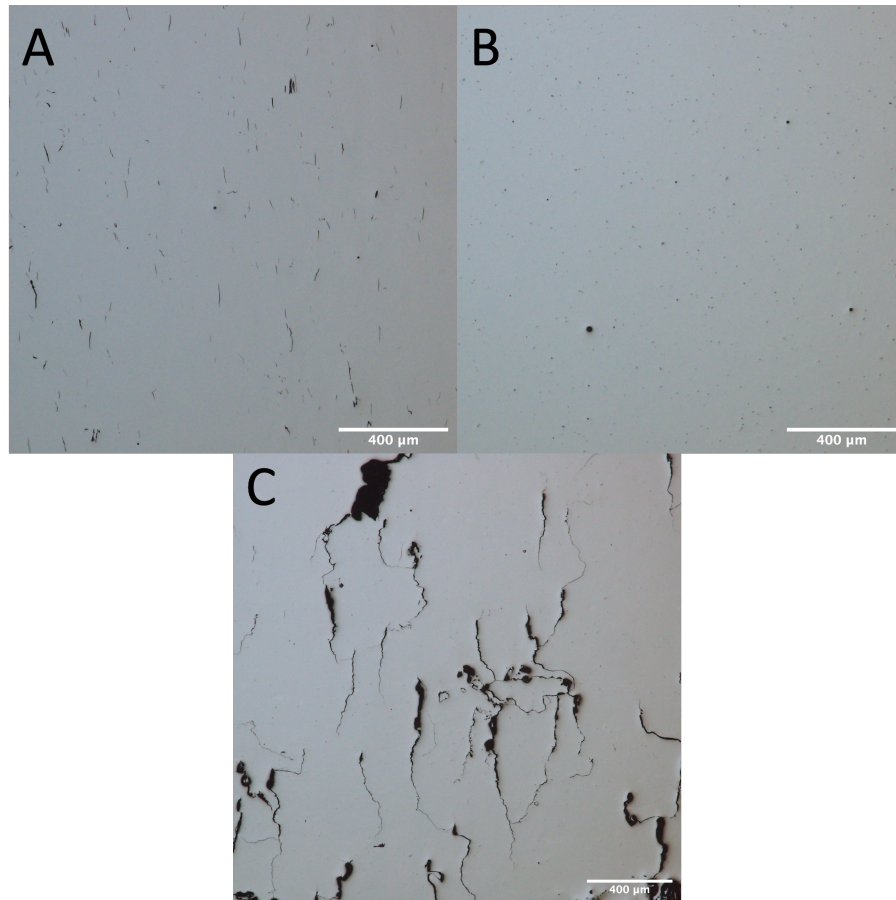
36G.6   Figures and Tables

Figure 36G.1: Light optical microscopy of LPBF of Haynes 230 A) with no inoculants B) 1wt% added inoculant A C) 2.66wt% added inoculant A.
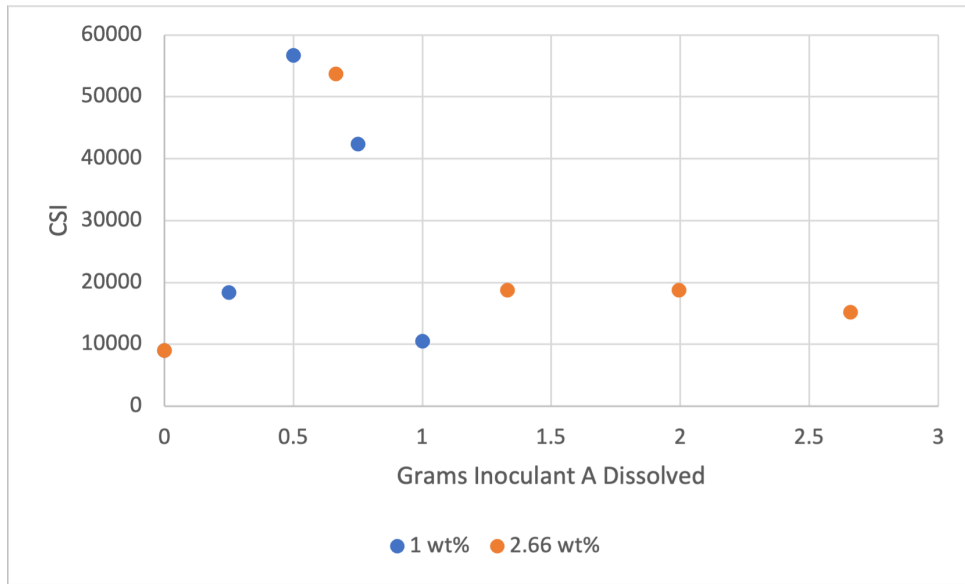
Figure 36G.2: Crack susceptibly index vs amount of inoculant A dissolved into Haynes 230.
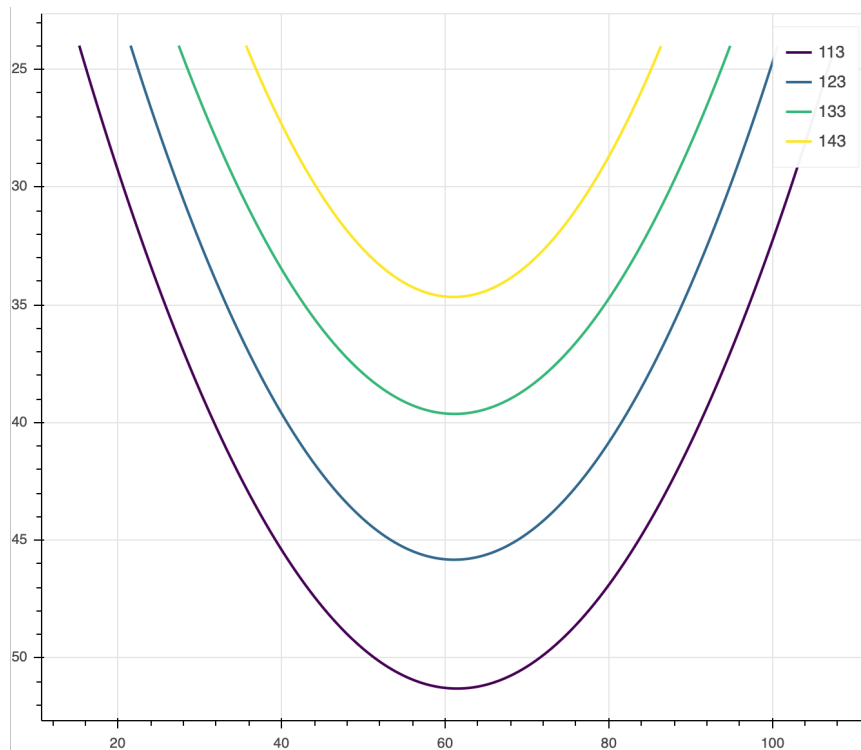

Figure 36G.3: Relative pixel location of solid/liquid interface at various frames for Inconel 738 at 108 Watts.
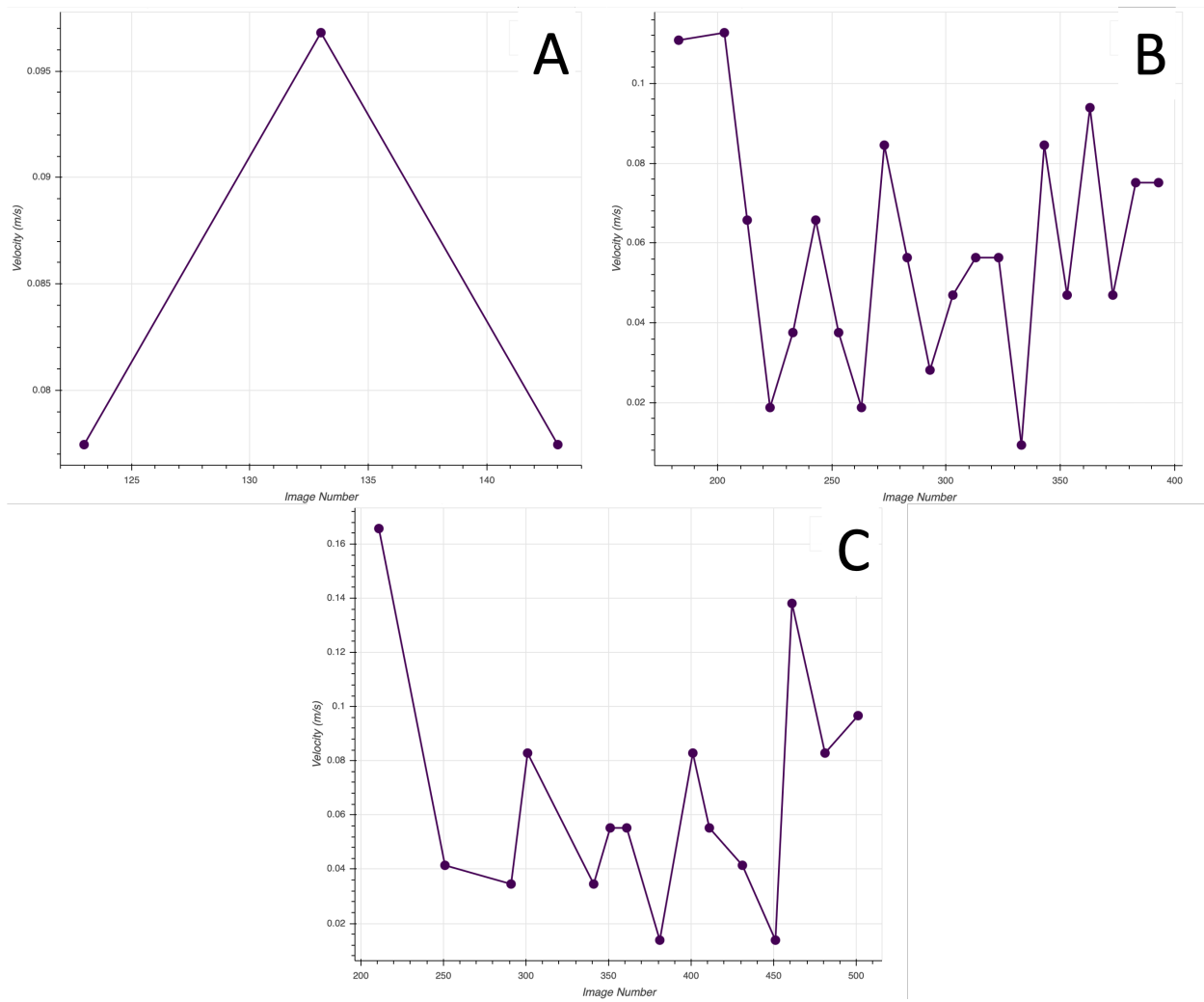
Figure 36G.4: In-situ solidification velocity of Inconel 738 spot melts at A) 108 Watts B) 216 Watts C) 324 Watts.

Table 36G.1: Final Flow3D values and assumptions used to model an Inconel 718 spot weld.

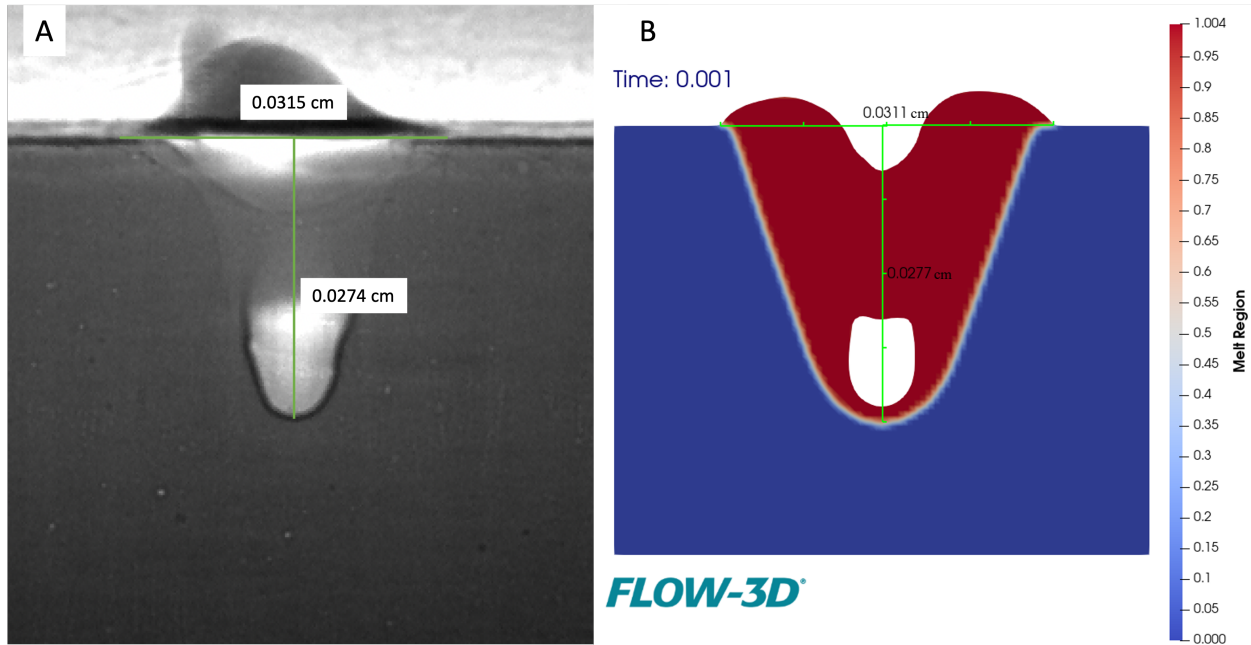|	
Accommodation Coefficient of Evaporation	0.1
Rising Pressure Magnification	0.1
Fluid Absorption Rate	0.6
Laser Spot Radius (cm)	0.0025

Figure 36G.5: Dimensional comparison of X-ray radiography and simulated spot melt.
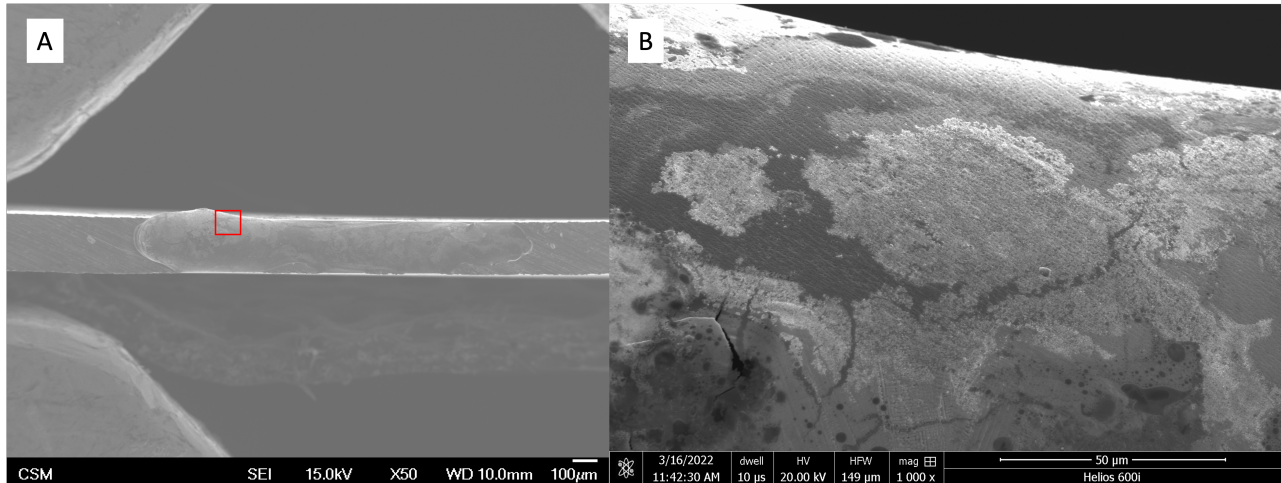

Figure 36G.6: Top-down SEM imaging of raster melt on Inconel 718 powder at A) 50x to verify raster position B) 1000x to observe dendritic orientation along the surface.
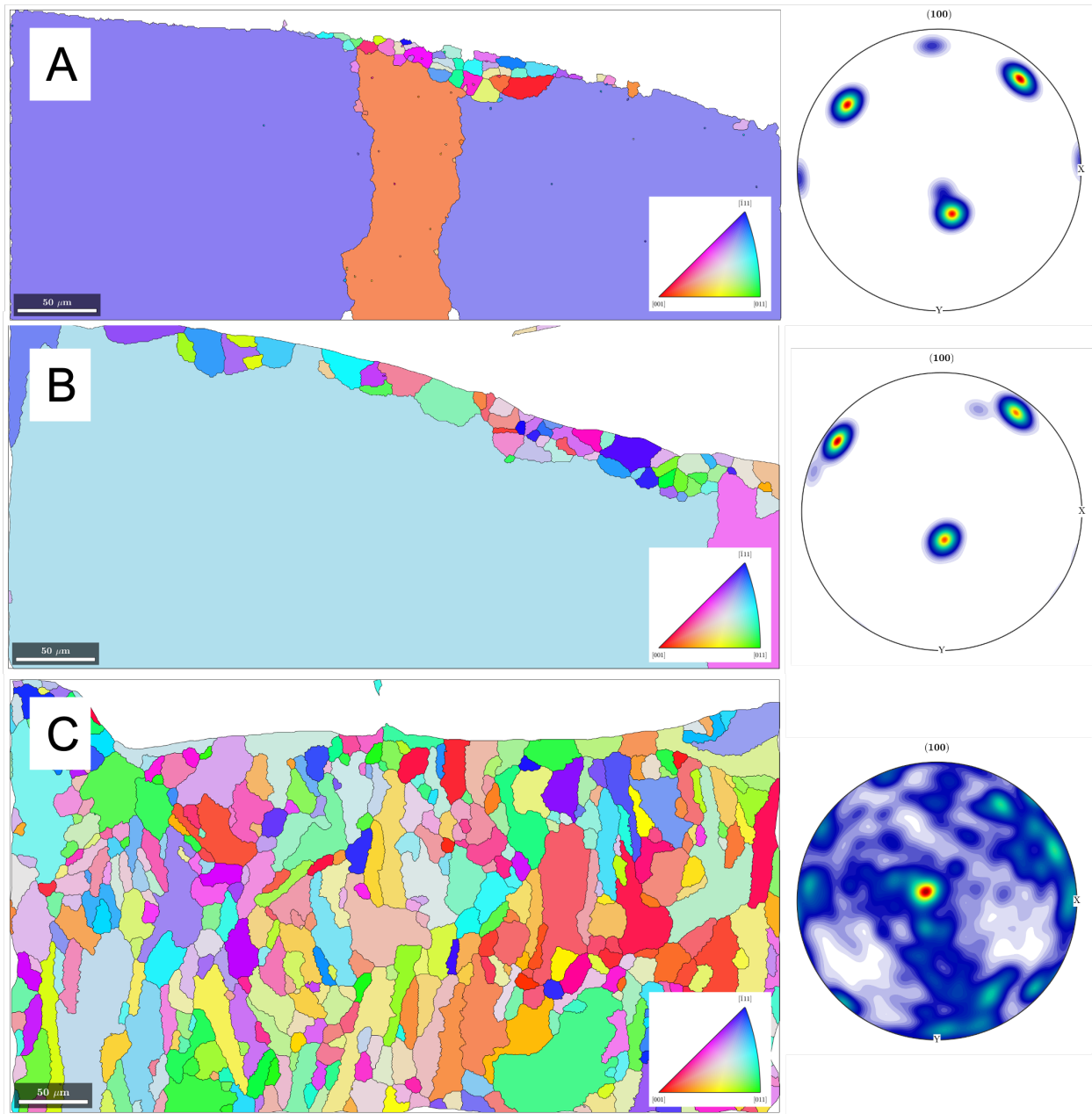
36G.7

Figure 36G.7: Inverse Pole Figure (IPF) map and Orientation Distribution Function (ODF) near the end of a raster of Inconel 718 with A) columnar base with nominal Inconel 718 powder B) columnar base with inoculated powder C) inoculated base with inoculated powder.

36G.8